Space Weather

RESEARCH ARTICLE
10.1029/2021SW002798

Qualitative and Quantitative Assessment of the SET HASDM Database

Richard J. Licata[1], Piyush M. Mehta[1], W. Kent Tobiska[2], Bruce R. Bowman[2], and Marcin D. Pilinski[3]

[1]Department of Mechanical and Aerospace Engineering, West Virginia University, Morgantown, WV, USA, [2]Space Environment Technologies, Pacific Palisades, CA, USA, [3]Freestream, Boulder, CO, USA

Key Points:

- We conduct principal component analysis of High Accuracy Satellite Drag Model (HASDM) and JB2008 database covering almost two solar cycles
- HASDM models the movement of lighter species during solar minimum conditions
- HASDM exhibits the ability to capture/model NO and CO_2 cooling mechanisms

Correspondence to:
R. J. Licata,
rjlicata@mix.wvu.edu

Citation:
Licata, R. J., Mehta, P. M., Tobiska, W. K., Bowman, B. R., & Pilinski, M. D. (2021). Qualitative and quantitative assessment of the SET HASDM database. *Space Weather*, *19*, e2021SW002798. https://doi.org/10.1029/2021SW002798

Received 12 MAY 2021
Accepted 2 AUG 2021

Abstract The High Accuracy Satellite Drag Model (HASDM) is the operational thermospheric density model used by the US Space Force Combined Space Operations Center. By using real-time data assimilation, HASDM can provide density estimates with increased accuracy over other empirical models. With historical HASDM density data being released publicly for the first time, we can analyze the data to compare dominant modes of variability in the upper atmosphere as modeled by HASDM and the Jacchia-Bowman 2008 Empirical Thermospheric Density Model (JB2008), a Jacchia family model upon which density corrections are made as a part of the HASDM framework. This model comparison is conducted through the use of principal component analysis (PCA) which shows the increased variability of the HASDM dataset. We highlight HASDM's ability to capture the movement of lighter species during solar minimum conditions, unlike many empirical models. We then compare density from both models to the CHAllenging Minisatellite Payload (CHAMP) and Gravity Recovery and Climate Experiment (GRACE) accelerometer-derived density estimates. This comparison shows that HASDM more closely matches the accelerometer-derived densities with mean absolute differences of 30.93% compared to CHAMP and GRACE-A, respectively. The comparison also reveals improved representation of cooling mechanisms due to NO and CO_2 by the HASDM database.

Plain Language Summary Many density models for the upper atmosphere have been developed using data from various sources to fit parametric equations. These are classified as empirical models which make up a large portion of those used in operations. While they are generally reliable, there are conditions where their accuracy falls short, such as during geomagnetic storms or during periods of low solar activity. The High Accuracy Satellite Drag Model (HASDM) uses observations from calibration satellites to make real-time corrections (a process known as Dynamic Calibration of the Atmosphere) to density outputs from an empirical model, making it far more robust. In this paper, we analyze a 20 year dataset of HASDM outputs and compare it the baseline JB2008 model, upon which data is assimilated. By leveraging a mathematical tool called principal component analysis, we identify features in the HASDM dataset that are not modeled by JB2008, such as the movement of lighter species during solar minimum conditions. We also perform a case study where we compare both model outputs to high-fidelity density observations from different satellites during two unique periods. Through this comparison, we find evidence that the HASDM dataset captures the effects of NO and CO_2 cooling mechanisms.

1. Introduction

The challenge of accurately modeling thermospheric mass density over a multitude of conditions has severe repercussions in the context of orbit determination and Space Situational Awareness (SSA). Operators rely on these density models for decision making in regards to collision avoidance operations, where inaccuracies and uncertainties can have direct consequences. Insufficient knowledge of future satellite position can result in a collision between two objects. A potential collision would drastically increase the number of objects in a given orbital regime, increasing the probability of future collisions. This could result in a cascade, known as Kessler Syndrome (Kessler & Cour-Palais, 1978), which could make certain orbital regimes inaccessible. In an effort to avoid this, we look to improve our modeling and forecasting capabilities. A significant improvement in model accuracy came from the implementation of real-time data assimilation, notably utilized by the High Accuracy Satellite Drag Model (HASDM).

The thermosphere is a dynamic, highly driven system impacted by external forces (e.g., space weather events) and internal dynamics (e.g., species transport). Solar irradiance is a major source of variation, providing the baseline average density (Qian & Solomon, 2012). This process is well-represented by solar indices, particularly at low latitudes (Vickers et al., 2014). However, these indices are not adequate in characterizing the thermosphere during solar minimum (Bowman et al., 2008), when composition changes and other processes become more relevant (Mehta et al., 2019). During events like solar flares or coronal mass ejections, mass and energy from the Sun interact with the magnetosphere causing Joule heating and auroral particle precipitation into the thermosphere (Deng et al., 2013; Fedrizzi et al., 2012). This causes sudden and often large changes in mass density. Due to a lack of pre-storm conditioning, empirical models frequently under-perform during these events (Bruinsma et al., 2021). The thermosphere consists of multiple neutral species that are influenced by these processes. Global circulation causes interhemispheric transport of lighter species resulting in latitudinal variations in species and neutral density (Qian & Solomon, 2012). In addition to horizontal species movement, upwelling and downwelling can transport species vertically impacting neutral density as a function of altitude. Horizontal and vertical transport mechanisms have been recently investigated by Sutton (2016). Certain species (e.g., nitric oxide (NO) and carbon dioxide (CO_2)) provide cooling mechanisms, particularly in response to geomagnetic activity (Houghton, 1970; Kockarts, 1980; Mlynczak et al., 2003).

Over the past six decades, the scientific community has developed and advanced thermospheric density models. A significant subset of these models are empirical. Empirical models use long-term trends from measurements over an array of instruments to fit parametric equations that describe the system. Even within this subset, there are multiple families/series of models that use different types of measurements and have evolved over decades. Three of these series, discussed by Emmert (2015), are the mass spectrometer incoherent scatter radar (MSIS; Picone et al., 2002), DTM (Bruinsma, 2015), and Jacchia series (Bowman et al., 2008). MSIS models typically use mass spectrometer and incoherent scatter radar measurements but have evolved and now incorporate additional data (e.g., accelerometer-derived density estimates). The Drag Temperature Model (DTM) series used orbit-derived density data but more recently incorporated accelerometer-derived density and mass spectrometer data. The Jacchia series of models (e.g., Jacchia-70 and the Jacchia-Bowman 2008 Empirical Thermospheric Density Model (JB2008)) strictly use both orbit- and accelerometer-derived density estimates. The availability of accelerometer-derived density estimates has been advantageous for model development and assessment. Over the lifetime of satellites with on board accelerometers (e.g., CHAllenging Minisatellite Payload (CHAMP) and Gravity Recovery and Climate Experiment (GRACE)), we accumulate measurements over many altitudes and space weather conditions (Bettadpur, 2012; Luhr et al., 2002). Researchers have used these measurements to derive density estimates by removing accelerations from other sources (e.g., gravity and solar radiation pressure, SRP; Calabia & Jin, 2016b; Doornbos, 2012; Mehta et al., 2017; Sutton, 2008).

HASDM was developed by Storz et al. (2005) and is an assimilative extension of the Jacchia (1970) upper atmosphere density model. HASDM employs dynamic calibration of atmosphere (DCA) which uses calibration satellite observations to make corrections to its background empirical density model. This assimilation technique was introduced as an application for HASDM by Casali and Barker (2002), but was expanded later to estimate 13 global density correction parameters (Storz et al., 2005). HASDM is not available for public use, but the global density outputs from the model were recently released to the public for the first time by Space Environment Technologies (SET; Tobiska et al., 2021). It is called the SET HASDM density database. This database contains three-dimensional (3D) density grids from the start of 2000 to the end of 2019 at a 3-h cadence. The HASDM dataset has a spatial resolution of 15° longitude, 10° latitude, and 25 km in altitude from 175 to 825 km.

In this work, we will leverage principal component analysis (PCA), also referred to in literature as empirical orthogonal function analysis or proper orthogonal decomposition, in order to study and compare the most dominant sources of variance within the HASDM dataset and spatiotemporally matched JB2008 model outputs. The resulting modes of variation and temporal coefficients give insight into the processes that drive the variance within the models. A similar methodology has been used to analyze thermospheric density datasets previously and is often used in the development of reduced-order models (Gondelach & Linares, 2020; Mehta et al., 2018; Mehta & Linares, 2017). PCA has also been used to study satellite

accelerometer datasets (Calabia & Jin, 2016b; Lei, Matsuo, et al., 2012; Matsuo & Forbes, 2010). For this article, the use of PCA is restricted to a quantitative (determining correlation) and qualitative (examining modes and coefficients) investigation.

This article is organized as follows, we start by detailing the HASDM and JB2008 models and their drivers. Then, we discuss the use of PCA as an investigatory tool followed by the results of the analysis. After, we compare the HASDM and JB2008 densities to CHAMP and GRACE density estimate over the entire availability of their measurements, with a focus on storm-time and quiet conditions.

2. Models, Data, and Methods

2.1. JB2008

The most recent in the Jacchia series is the JB2008 density model. JB2008 was an improvement to its predecessors and incorporated new solar and geomagnetic indices to drive the model. It uses the F_{10}, S_{10}, M_{10}, and Y_{10} indices and proxies to model variations caused by solar heating. In addition to a_p, JB2008 utilizes *Dst* to improve model density during geomagnetic storms. These indices are used in temperature corrections, semiannual functions, and new *Dst* temperature equations. The model reduced non-storm density errors by $> 5\%$ and reduced storm-time density errors from Jacchia-70 by $> 60\%$, from NRLMSIS by $> 35\%$, and from JB2008 (with only a_p) by 16% (Bowman et al., 2008).

2.2. HASDM

Using JB2008 as the background density model, HASDM is able to further reduce these errors. By building on the density correction work of Marcos et al. (1998) and Nazarenko et al. (1998), HASDM can provide dynamic global density corrections via 13 global temperature correction coefficients through its DCA algorithm. HASDM also exploits a prediction filter for its DCA corrections. Through this filter, the model adjusts an extrapolated time series of 27 days (one solar rotation) for the correction coefficients using wavelet and Fourier analysis (Storz et al., 2005). For satellite trajectory estimation, HASDM uses a technique, called segmented solution for ballistic coefficient (SSB), that enables the estimated ballistic coefficient to deviate over the fitting period. At the time of the original HASDM publication, it used approximately 75 calibration satellites for fitting. As of 2001, the satellites spanned from 190 to 900 km in altitude with a majority being between 300 and 600 km (Bowman & Storz, 2003). The temperature correction coefficients produced by HASDM are not released to the public. However, SET recreates the HASDM output weekly for validation, and this recreation makes up the SET HASDM density database. For more details on HASDM, the reader is referred to Storz et al. (2005), and for more details on SET's validation and on the database, the reader is referred to Tobiska et al. (2021). While HASDM is an assimilative correction scheme to a background model, we refer to the SET HASDM dataset as a model for convenience.

2.3. Model Drivers

The most common solar proxy used in density modeling is $F_{10.7}$, referred to in this article as F_{10}. Originally identified and measured by Covington (1948), F_{10} serves as a proxy for solar extreme ultraviolet (EUV) emissions which deposit energy into the thermosphere. The 10.7 in the subscript refers to the 10.7 cm wavelength of the solar radio flux being measured. While this does not directly interact with the Earth's atmosphere, it has been shown to be a reliable proxy for thermospheric heating (Tobiska, Bouwer, & Bowman, 2008). F_{10} is measured in solar flux units ($10^{-22} Wm^{-2} Hz^{-1}$) indicated as *sfu*.

The S_{10} index characterizes the integrated 26–32 nm solar EUV emission, which penetrates into the middle thermosphere and is absorbed by atomic oxygen (Tobiska, Bowman, & Bouwer, 2008). While the emissions that S_{10} represents have no relationship to the 10.7 cm wavelength, they are normalized and converted to *sfu* through linear regression. Similar fits are done for M_{10} and Y_{10} to convert to uniform units. M_{10} is a proxy representative of far ultraviolet photospheric 160 nm Schumann-Runge Continuum emissions and is consistent with molecular oxygen dissociation in the lower thermosphere (Tobiska, Bowman, & Bouwer, 2008). The final solar driver for JB2008 is Y_{10}, which represents X-ray emissions in the 0.1–0.8 nm range and H Lyman-α 121 nm emissions. During solar maximum, the X-ray emissions are more heavily weighted, and

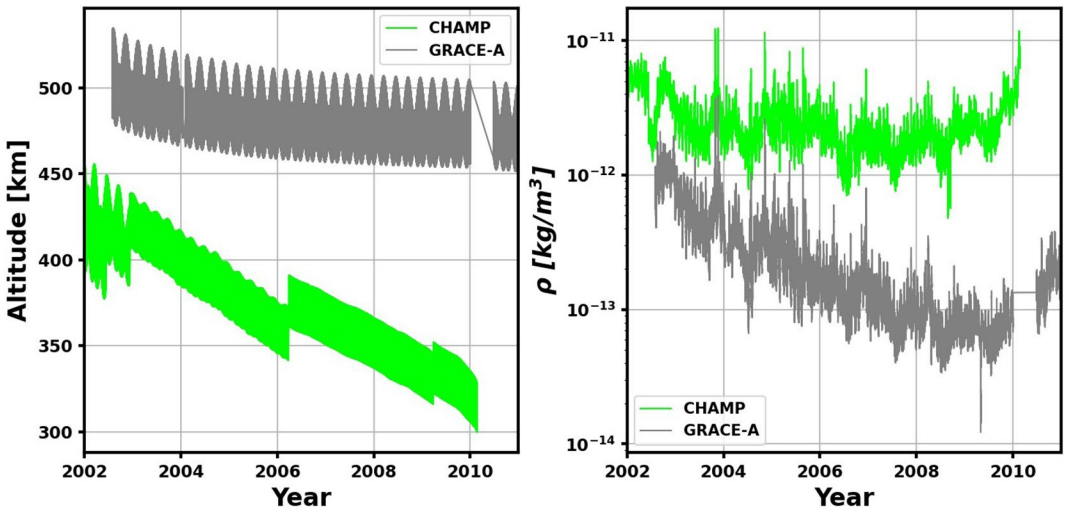

Figure 1. Altitude (left) and orbit-averaged densities (right) for CHAMP and GRACE-A.

the opposite is true for solar minimum. For each of these four solar drivers, 81-days centered averages are generated and used for prediction in JB2008.

The first of the two geomagnetic drivers for JB2008 is the geomagnetic planetary amplitude, a_p. It has a 3-h cadence and is often used in density models. However, using *Dst* during geomagnetic storms results in increased accuracy over a_p for density modeling (Bowman et al., 2008). The *Dst* index is largely driven by the strength of the ring current in the inner magnetosphere. This makes it an ideal indicator of ring current strength and therefore geomagnetic storms (Ganushkina et al., 2017).

For operational use of HASDM, forecasts of these drivers are required. SET provides the driver forecasts using multiple algorithms/sources. The solar drivers are forecasted using the *SOLAR2000* algorithm (Tobiska et al., 2000). a_p forecasts come from the National Oceanic and Atmospheric Administration Space Weather Prediction Center forecasters, and *Dst* forecasts are a produced by the *Anemomilos* algorithm (Tobiska et al., 2013). Error statistics of historical forecasts for all six drivers were presented as a community benchmark by Licata et al. (2020).

2.4. CHAMP and GRACE Density Estimates

The CHAMP and GRACE datasets used in this study are from Mehta et al. (2017), which originate from Sutton (2008) but are scaled to account for higher fidelity satellite geometry and improved gas-surface interaction simulations (Mehta et al., 2013, 2014; Walker et al., 2014). However, there is no correction to the SRP accelerations which used the simplified 13-panel geometry. Both satellites have near polar orbits, covering nearly all latitudes, and over their respective lifetimes, CHAMP and GRACE datasets cover altitudes ranging from 300 to 535 km. This, in conjunction with the date range covered by the satellites, makes their density estimates invaluable for model comparison. Figure 1 shows altitudes each dataset covers along with orbit-averaged densities over their mission spans. This study only included CHAMP and GRACE-A data due to similarities between the orbits of GRACE-A and GRACE-B.

The orbit-averaged densities were computed using a centered window with a span of 90 min, approximately one orbit. Discontinuities in Figure 1 represent data gaps. Both the CHAMP and GRACE-A datasets contain files for every day containing information such as GPS time, local solar time, latitude, altitude, and density. CHAMP has measurements every 10 s, while GRACE-A provides measurements every 5 s.

2.5. Methodology

2.5.1. Principal Component Analysis

The spatial resolution of these models are 15° longitude, 10° latitude, and 25 km altitude spanning from 175 to 825 km. This results in 12,312 grid points for every 3 h between the start of 2000 to the end of 2019. The high dimensionality of the data makes it a prime candidate for PCA. PCA is an eigen decomposition technique that determines uncorrelated linear combinations of the data that maximize variance (Hotelling, 1933; Karl Pearson, 1901).

PCA has been used in the last two decades on atmospheric density models and accelerometer-derived density sets alike. Matsuo and Forbes (2010) applied linear regression using spherical harmonics to extract the mean of CHAMP densities and performed PCA on the residuals, and Lei, Matsuo, et al. (2012) expanded this methodology to both CHAMP and GRACE data. Calabia and Jin (2016a) interpolated GRACE accelerations to a grid prior to performing PCA. This methodology was expanded to a 3D global grid by Mehta and Linares (2017) and is used in this work.

For both models, the spatial dimensions are reshaped into a single dimension to make the spatiotemporal dataset two-dimensional. Then a common logarithm of the density values is taken in order to reduce the variance of the dataset from five orders of magnitude to less than one. To examine the inherent differences between HASDM and JB2008, the difference (HASDM − JB2008) is taken between the log-density values across the spatial and temporal dimensions for a separate analysis. Next, we subtract the temporal mean for each cell to center the data. Finally, we perform PCA using the *svds* function in *MATLAB* to obtain the U, Σ, and V matrices. PCA decomposes the data and separates spatial and temporal variations such that:

$$\mathbf{x}(\mathbf{s},t) = \bar{\mathbf{x}}(\mathbf{s}) + \tilde{\mathbf{x}}(\mathbf{s},t) \quad \text{and} \quad \tilde{\mathbf{x}}(\mathbf{s},t) \approx \sum_{i=1}^{r} \alpha_i(t) U_i(\mathbf{s}) \tag{1}$$

where $\mathbf{x} \in \mathbb{R}^n$ is the model output state (density on its full 3D grid), $\bar{\mathbf{x}}$ is the mean, $\tilde{\mathbf{x}}$ is the variance, r is the choice of order truncation, α_i are temporal coefficients, and U_i are orthogonal modes or basis functions. The modes are the first r columns of the left singular vector derived by performing PCA on an ensemble of model output solutions such that:

$$\mathbf{X} = \begin{bmatrix} | & | & | & & | \\ \tilde{\mathbf{x}}_1 & \tilde{\mathbf{x}}_2 & \tilde{\mathbf{x}}_3 & \cdots & \tilde{\mathbf{x}}_m \\ | & | & | & & | \end{bmatrix} \quad \text{and} \quad \mathbf{X} = U\Sigma V^T \tag{2}$$

In Equation 2, m represents the ensemble size (two solar cycles with HASDM and JB2008). The normalized and centered data is denoted by $\mathbf{X}$. U is the left unitary matrix, and it is made of orthogonal vectors that represent the modes of variation. Σ is a diagonal matrix consisting of the squares of the eigenvalues that correspond to the vectors in U. We can extract temporal coefficients by performing matrix multiplication between Σ and V^T. Therefore, the signs of the modes and coefficients are important in the analysis phase. The reader is referred to Bjornsson and Venegas (1997) for more details on the distinction between PCA and singular value decomposition for use on climatic data.

Upon obtaining the temporal coefficients, we compute the Pearson correlation coefficients between each driver and PCA coefficient (Pearson, 1920). In addition to the space weather drivers, the models use temporal inputs (e.g., universal time and day of year). To correlate seasonal and annual trends, we generated sinusoidal inputs based on the day of year (Weimer et al., 2020). The first two are sine and cosine functions with periods of 6 months. This is used to test correlations with semiannual trends. The last two are sine and cosine functions with periods of 1 yr to correlate with annual trends.

2.5.2. Model-Data Comparison

In order to compare the satellite density estimates to the two models, we implement a trilinear interpolation algorithm using the global density grids from the models. Since the temporal resolution of the model densities is only every 3 h, we maintain the same density grids over each 3-h period and interpolate the

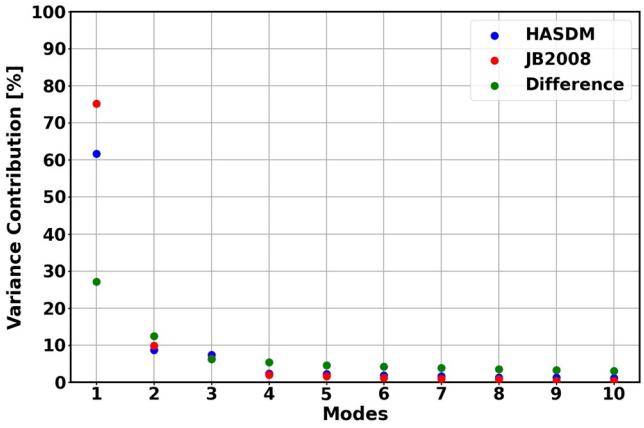

Figure 2. Percentage of variance captured by the 10 most energetic modes.

model densities to the satellite positions at their respective cadence (5 or 10 s). The authors appended the existing CHAMP and GRACE density data of (Mehta et al., 2017) with the HASDM and JB2008 densities and have made them publicly available to the community (see Data Availability Statement section).

$$\text{Mean absolute percent difference} = mean\left(100\%\frac{\left|\rho_{model}-\rho_{satellite}\right|}{\rho_{satellite}}\right) \quad (3)$$

We compute mean absolute percent difference shown in Equation 3 between the models and satellites using a 1-yr window to investigate the agreement between the four density sources (HASDM, JB2008, CHAMP, and GRACE-A). This is done for the individual density values and the orbit-averaged density values. Differences in the individual density values give an idea of localized deviations in the datasets while differences in the orbit-averaged density values represent the general deviations in the datasets. We also perform two case studies to compare densities during the 2003 Halloween Storm and a quiet period in 2009. There is no scaling performed on the densities, because the goal is to compare relative trends in the density data. Therefore, drag coefficient uncertainty can play a role in biases between models.

3. PCA Results

We begin by performing PCA on the entire dataset (2000–2020) to get insight into the general density formulations. Then, we look into specific conditions, such as solar maximum and solar minimum, where different processes drive the global density variations. In the solar maximum and solar minimum analyses, PCA is not conducted again on those individual years, we calculate the correlations for only the selected period.

3.1. 2000–2020, Solar Maximum, Solar Minimum Analysis

Figure 2 shows the variance captured by the first 10 modes of variation for the $\log_{10}$ HASDM and JB2008 densities. We also spatiotemporally decompose the difference between the HASDM and JB2008 model output to investigate the additional modes of variation within the HASDM database. Figure 2 also shows the variance captured by the first 10 modes of the differenced dataset. Note that the $\log_{10}$ density differences are taken prior to conducting PCA; therefore, it serves as a stand-alone analysis and will be discussed in Section 3.2.

It is clear that the contribution of the first PC for both models is significant, capturing over 60% of the system's total variance. More importantly, the first PC for JB2008 captures over 10% more variance than it does for HASDM. There is also more variance captured by the second PC for JB2008, but beyond that, the individual variance captured is marginally greater for HASDM. JB2008 densities are more generalized relative to HASDM. Therefore, PCA can capture more variance in the first few modes while HASDM contains more variability, spreading out the variance captured over an increased number of modes.

Figures 3–5 display the first five modes of variation for HASDM, the first five modes for JB2008, and the associated temporal coefficients for 2000–2020, respectively. Figures 6 and 7 show the temporal coefficients for 2001 (solar maximum) and 2019 (solar minimum), respectively. Figure 8 shows the results from a Pearson's correlation coefficient analysis between the drivers and temporal coefficients (α_i). The left, center, and right sections shows the results for 2000–2020, 2001 only, and 2019 only, respectively, while the top and bottom sections show the results for HASDM and JB2008, respectively. For the analysis of the individual years, the correlation coefficients are re-computed using only drivers and coefficients over a year-long window.

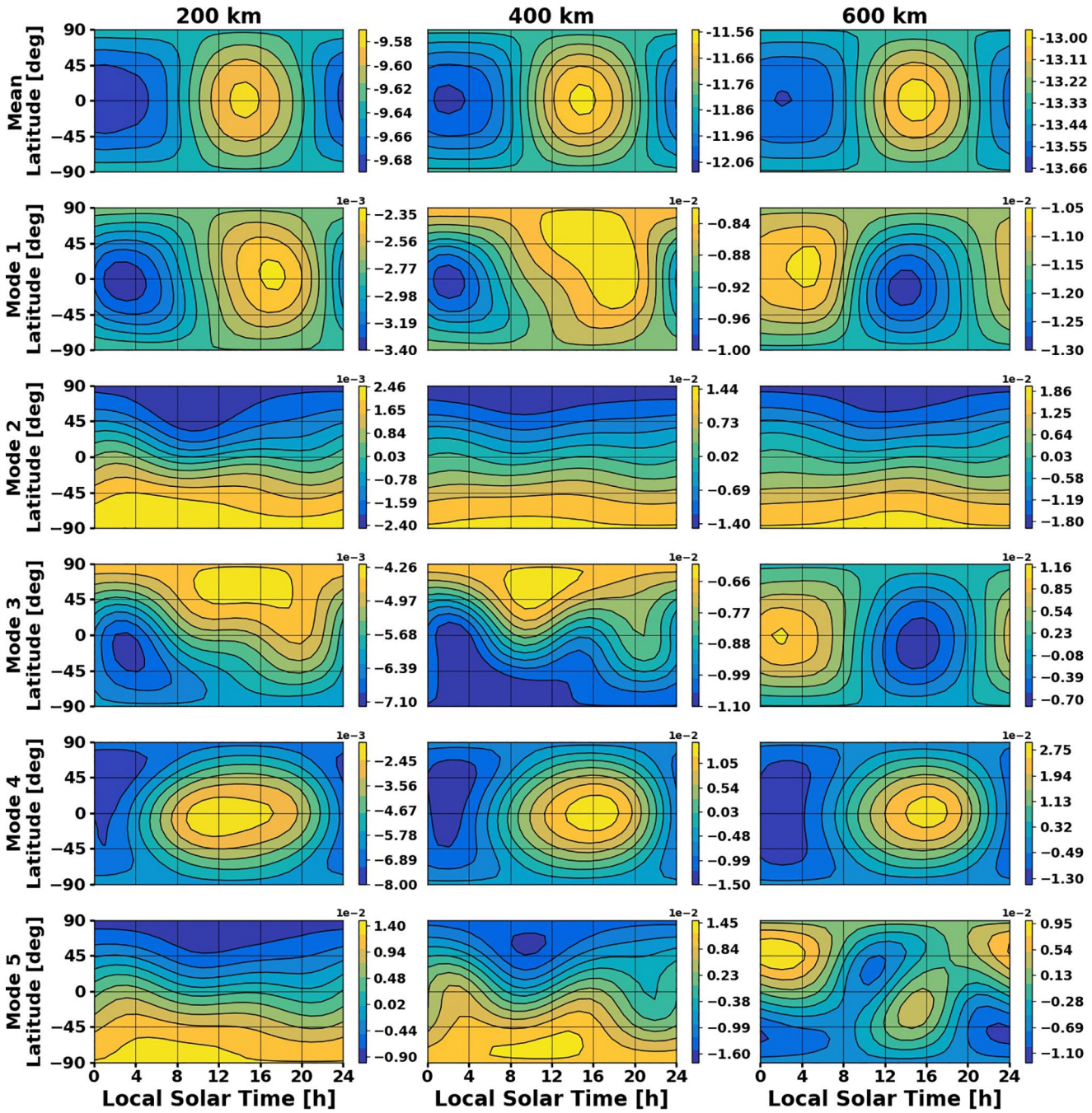

Figure 3. Mean $\log_{10}$ density and first five modes for HASDM at 200, 400, and 600 km.

The mean $\log_{10}$ density is shown in the first row of Figures 3 and 4 even though they are removed prior to performing PCA. The first mode for both models largely represents the solar flux cycle and is driven by temperature. There is a peak around 14 h local time and a minimum at 2 h. From Figure 8, the first coefficient is highly correlated to F_{10} and the other solar indices; there is a 90% or greater correlation to all four solar indices/proxies and their centered averages. There is lower correlation between α_1 and the solar drivers when considering only solar maximum or solar minimum. In these periods, there are higher correlations to the geomagnetic and temporal drivers. Between 400 and 600 km, mode 1 for HASDM flips peak locations; the transition occurs at 525 km. This is hypothesized to be the oxygen to helium transition

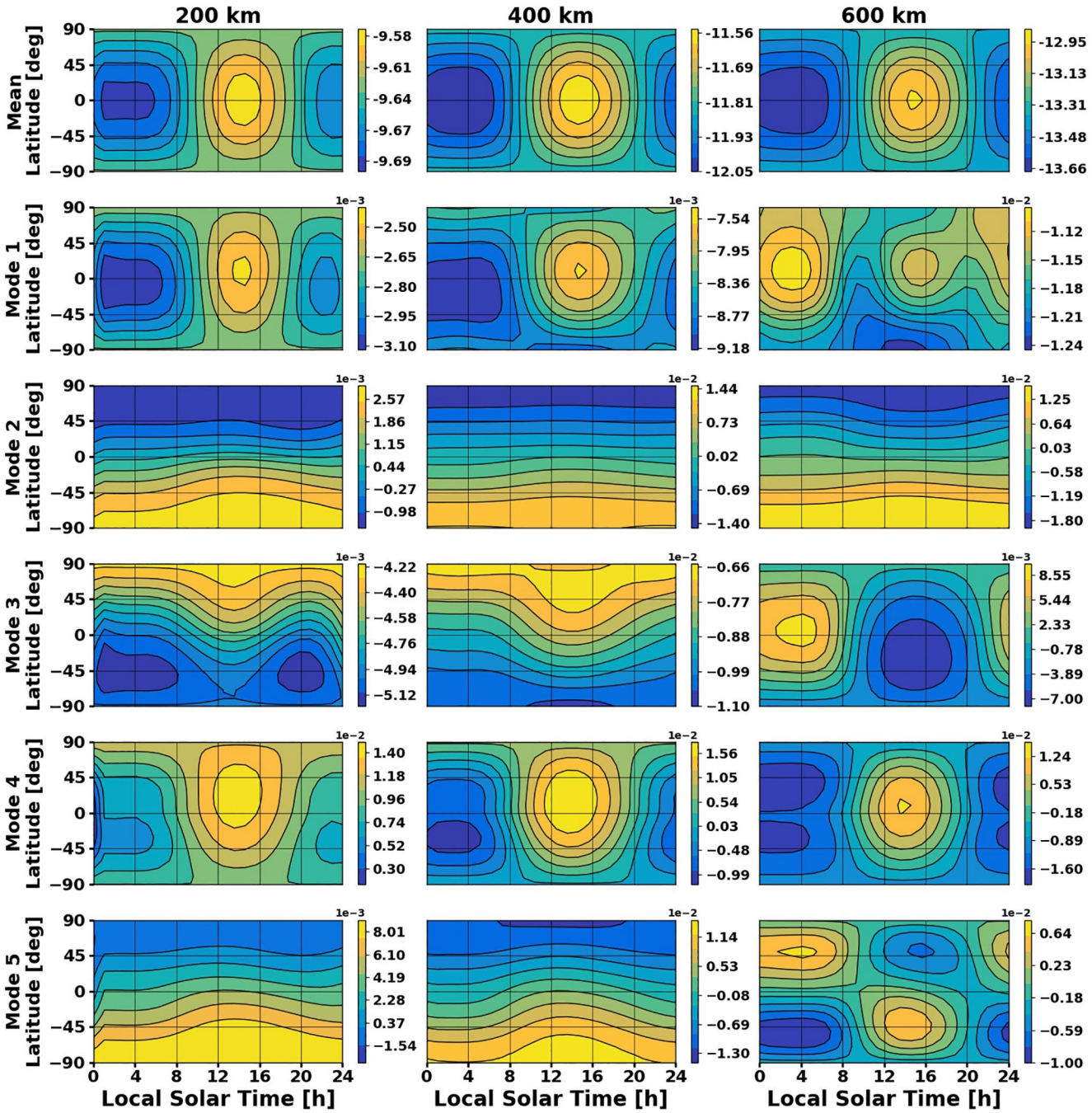

Figure 4. Mean $\log_{10}$ density and first five modes for JB2008 at 200, 400, and 600 km.

(Thayer et al., 2012) as lighter species have an inverse correlation to temperature (Mehta et al., 2019). This is also represented in JB2008, but it occurs at 600 km which can be seen in Figure 4. The second mode seemingly represents a hemispherical/latitudinal variation due to summer-winter variation. Based on the day of year, this mode can change in intensity and orientation. This is caused by the sinusoidal trend of α_2 with a period of ~ 365 days. There is a stronger signal in α_2 for JB2008 highlighting the increased variability in the HASDM dataset.

It is important to note that PCA does not guarantee that each mode represents physical processes or that a given mode corresponds to a single process. For the first two modes, there is an evident dominant process

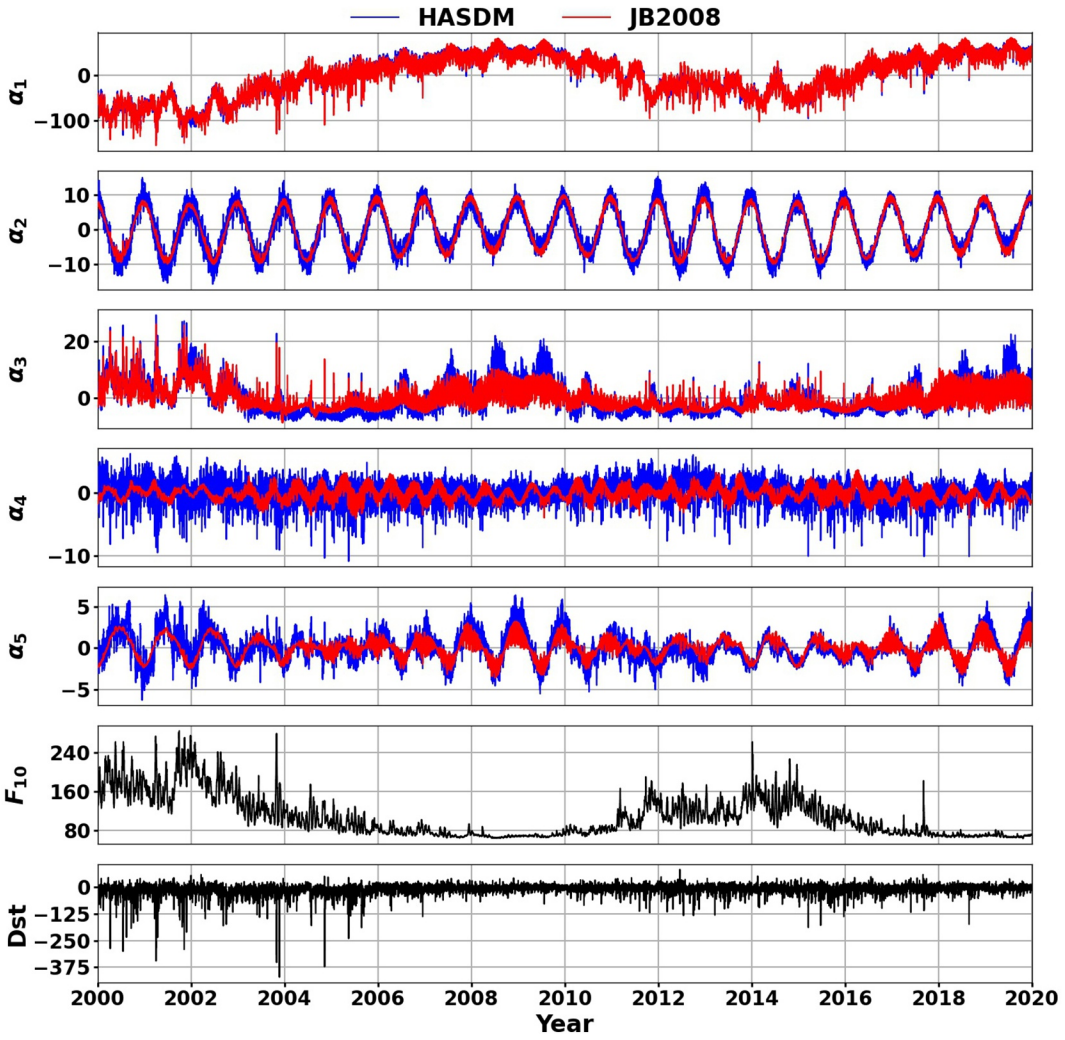

Figure 5. Temporal coefficients for both HASDM and JB2008 across two solar cycles.

representing it but does not seem to be the case for mode 3 based on the correlation values in Figure 8. In Figure 6, α_3 is nearly a mirror image of the first coefficient for both HASDM and JB2008, visually. However, Figure 7 shows that there are no longer strong similarities between α_1 and α_3. The general appearance of α_3 in 2019 is even different between the two models. These observations are reinforced by the correlation values in Figure 8 for α_3 during the three periods. There are negligible correlation values for the entire period, but the coefficient correlates strongly with different drivers during solar maximum and solar minimum.

In Figures 3 and 4, the movement of the peak in mode 3 provides insight to HASDM. At lower altitudes (200–400 km), the HASDM peak has a ~ 4 hour shift relative to JB2008. The JB2008 peak is located between 12 and 14 h local time while HASDM's are around 9 h. Beyond 400 km, the peak in both models shifts to 2 h local time and toward the equator. They exhibit similar trends up to 825 km which hints at the reliance on HASDM's background model when the signal decreases at higher altitudes. We interpret this as HASDM's ability to accurately capture the winter helium budge prominent during solar minimum conditions (Keating & Prior, 1968; Reber & Hays, 1973) as the local time peak coincides with the high concentration of helium observed by Cageao and Kerr (1984) and Thayer et al. (2012) around 9 h local time.

The last two modes shown in Figures 3 and 4 for the two models are flipped, meaning the fourth for HASDM has the same source as the fifth for JB2008 and *vice versa*. There is only a 2.25% difference between modes 4 and 5 for HASDM which signifies that their respective contribution to the system's overall variance is

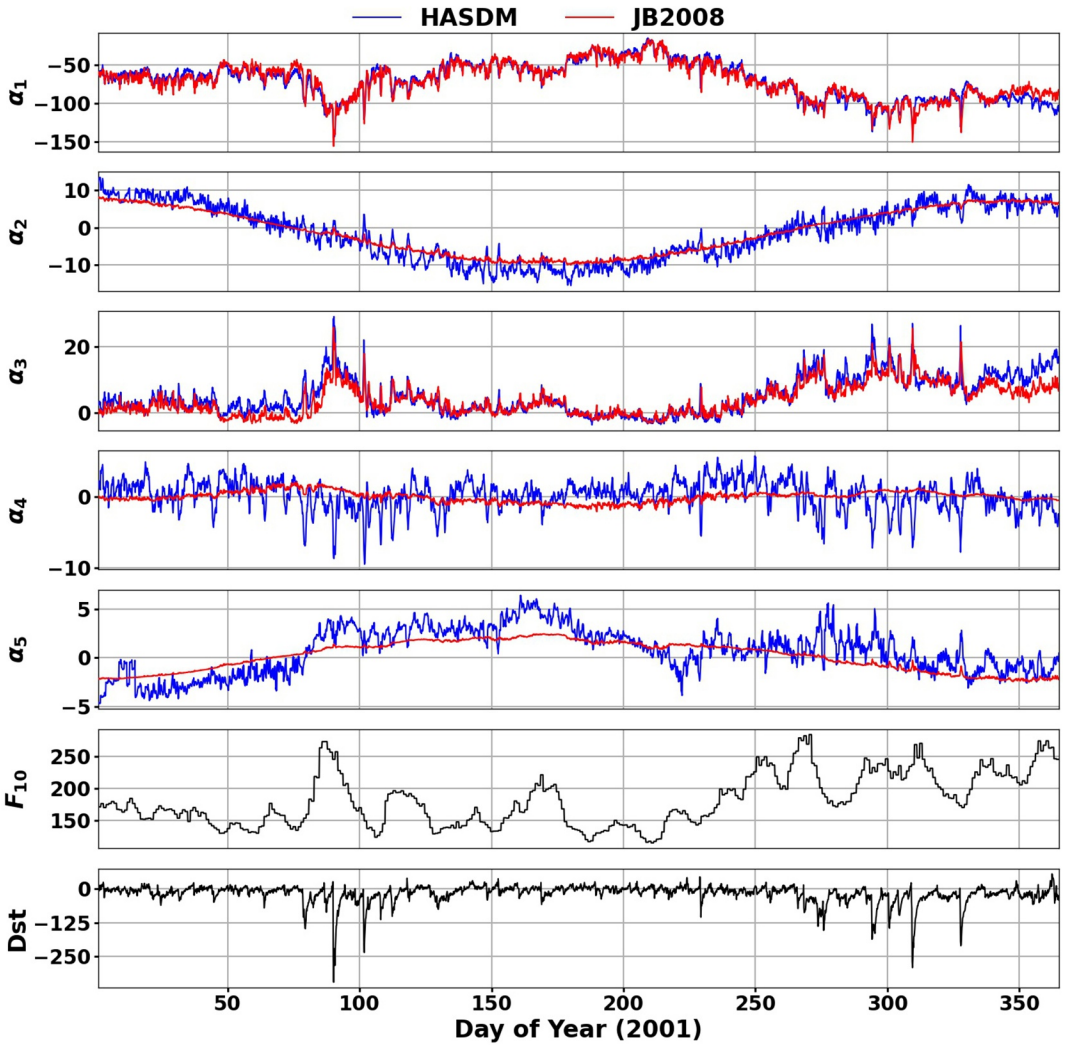

Figure 6. Temporal coefficients for both HASDM and JB2008 for 2001.

similar. Therefore, in all mode and coefficient figures, we switch JB2008 modes 4 and 5 to have them match that of HASDM.

Mode 4 seems to be further effects of solar heating, while mode five is similar to mode three in its structure. α_4 has some correlation to geomagnetic activity, while α_4 for JB2008 has moderately strong correlation to the semiannual cosine wave. In Figures 3 and 4, the difference between modes 3 and 5 is the location of the peak present in either the northern or southern poles.

During all three periods, α_4 for JB2008 has a high correlation with the semiannual cosine wave (around −0.70), while α_4 for HASDM has its highest correlation with a_p and *Dst*. In the coefficient figures, α_4 for HASDM has spikes that coincide with the geomagnetic storms seen in the *Dst* plot. α_5 for both models have high correlations with the annual cosine wave and likely represent residuals from the summer-winter variation.

3.2. Density Difference PCA

Figure 9 shows the mean $\log_{10}$ density difference and the first three modes from the density difference PCA at 200, 400 and 600 km. Figure 11 contains the correlation coefficients between the drivers and temporal coefficients for the difference analysis. The temporal coefficients for this analysis can be found in Figure 10.

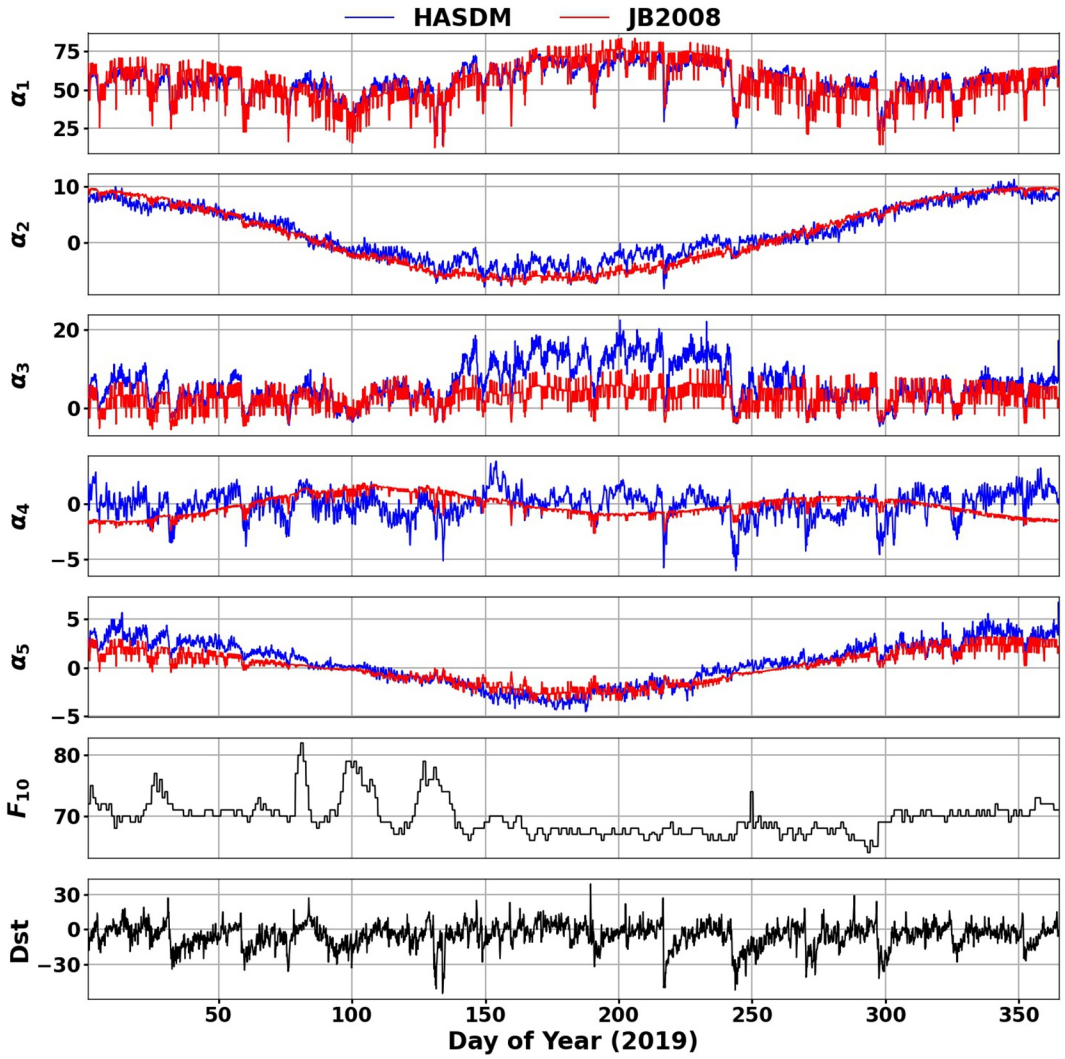

Figure 7. Temporal coefficients for both HASDM and JB2008 for 2019.

The first row in Figure 9 contains the mean density differences at three altitudes. These show that the diurnal structure of the models' densities deviate from one another, particularly with respect to altitude. The color bar limits are centered around zero showing that HASDM predicts higher night-side densities and lower dayside densities. The specific structure of this difference evolves with altitude.

The first mode is representative of the additional variation captured in α_1 for HASDM relative to JB2008. While Figure 11 shows no meaningful correlation between α_1 and the solar drivers, Mode 1 has peaks at ~14 h and a general diurnal structure. Considering how α_1 oscillates about zero in the first column of Figure 10, the first mode is likely representative of structural differences in density related to the expansion of the thermosphere. In the last column of Figure 10, α_1 has a semiannual period, supported by its correlation with the semiannual cosine wave (−0.37).

Figure 11 shows that α_2 correlates to all the solar drivers, and has some correlation with the geomagnetic and temporal drivers. In the first column of Figure 10, α_2 is mostly negative during solar maximum and does not have any significant long-term trends during those periods. However, during solar minimum, it oscillates above zero with a defined semiannual period, as seen in the last column. This suggests that it may represent a process that is prevalent during solar minimum.

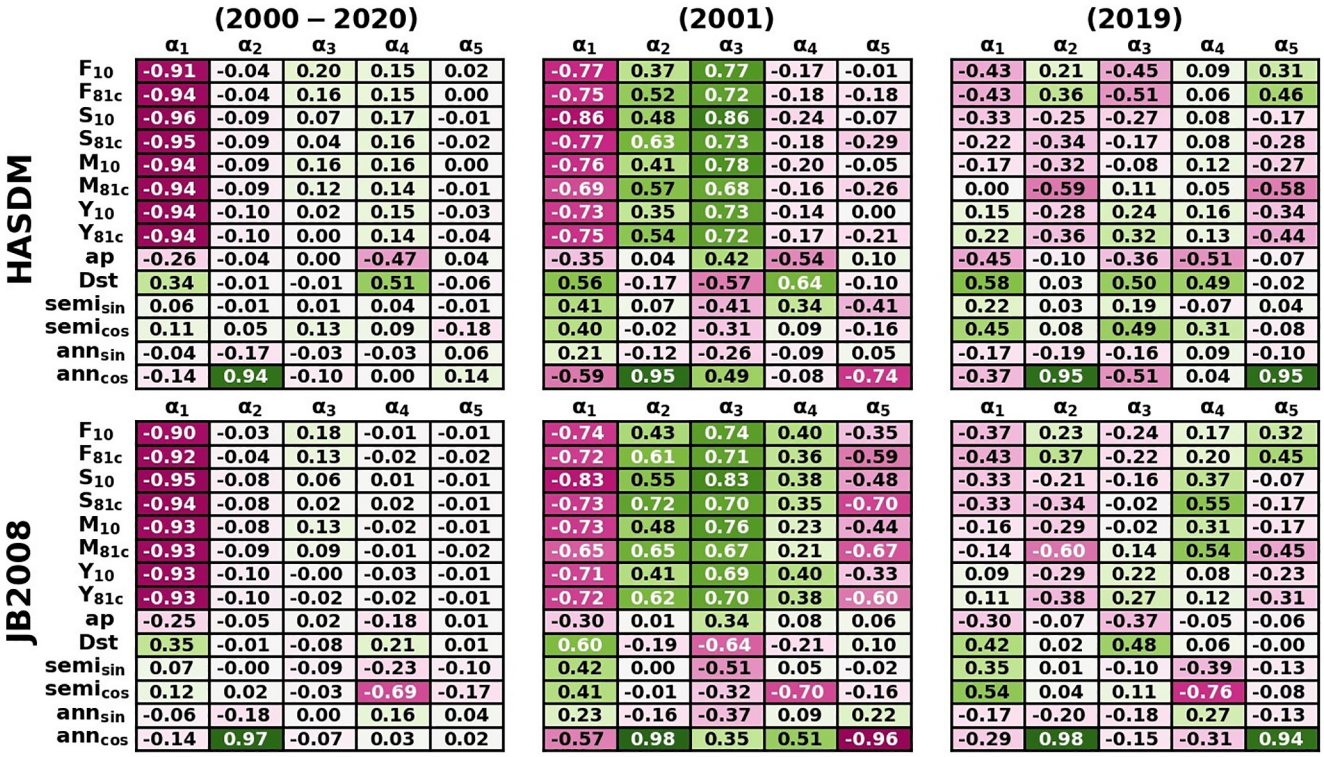

Figure 8. Heat map of the Pearson correlation coefficients between all inputs and the first five temporal coefficients for: 2000–2020 (left), 2001 only (center), and 2019 only (right). HASDM and JB2008 are shown in the top and bottom sections, respectively.

There is an interesting structural evolution for mode two in Figure 9 with increasing altitude. Based on the peak and trough locations at 600 km, we hypothesize that it represents the movement of lighter species during solar minimum. Lighter species rise through vertical advection and move laterally through horizontal divergence and advection (Sutton, 2016). Looking at the 600 km profile for mode 2, there is a trough centered above the equator at 14 h, where density is highest due to heating. α_2 is positive during solar minimum, holding the peak-trough locations, and negative during solar maximum, flipping the peak-trough locations. Mode 2 during solar maximum would revert to a simple heating profile.

In Figure 9, mode 3 shows a latitudinal dependence with asymmetry between the poles. α_3 in Figure 10 changes with the seasons, which follows the interhemispheric transport of light species (Mehta et al., 2019). The modes in Figure 9 and the temporal coefficients in Figure 10 come from the density difference analysis, meaning it is representative of a process in only one of the models. Most empirical models, like JB2008, use diffusive equilibrium to predict temperature as a function of altitude, which does not take into account the profiles of the individual species (Picone et al., 2016). The technique breaks down during solar minimum when the movement of lighter species becomes critical. We hypothesize that HASDM is able to capture this phenomenon.

4. Model-Satellite Density Comparison

Figure 12 shows histograms of the log_{10} orbit-averaged densities for both satellites and models, and Table 1 shows mean absolute differences for both the orbit and orbit-averaged densities with respect to the satellite densities, broken down by year. Both HASDM and JB2008 overpredict density relative to CHAMP and GRACE-A. However, the HASDM distributions have a marginally smaller bias for both satellites. The shape of the HASDM distributions more closely matches the high fidelity CHAMP and GRACE-A estimates with the smaller peaks being present on the right side. The JB2008 has similar distributions to both satellites but

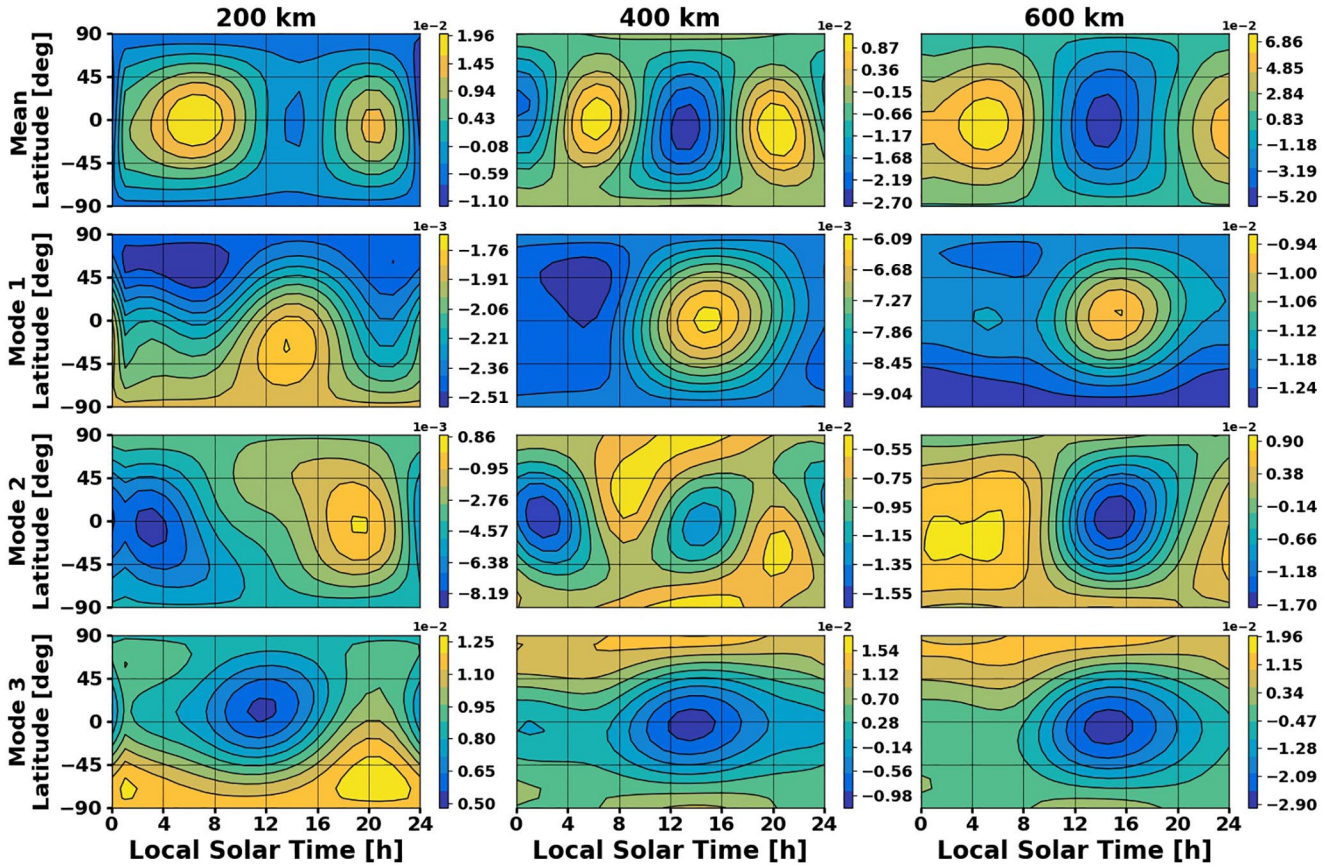

Figure 9. Mean $\log_{10}$ density difference and first three modes for the density differences at 200, 400, and 600 km.

appears more generalized. Possible sources for the biases can include imperfect drag coefficient (c_D) (Mehta et al., 2014; Walker et al., 2014) and SRP (Vielberg & Kusche, 2020) modeling.

HASDM densities more closely match both CHAMP and GRACE-A estimates overall. However, there are years for both satellites where JB2008 predicts densities closer to the satellite estimates, particularly as the solar cycle begins to transition out of solar maximum (2003–2004) and as it transitions out of solar minimum (2010). In general, there is more agreement between the model and satellite densities during solar maximum. The models have lower percent differences when looking at orbit-averaged values, because they are tracking general density trends much better than the short period disturbances. The decrease in the density differences range from 3 – 13% and 4 – 15% for HASDM and JB2008, respectively, when comparing the orbit to obit-averaged differences for CHAMP. For GRACE-A, the differences are more pronounced, being 5 – 20% for HASDM and 5 – 19% for JB2008. Considering the similarity in orbit inclination, this disagreement between the orbit and orbit-averaged differences may be attributed to the altitude.

5. CHAMP and GRACE Case Study

To more closely examine the densities, we look at both active and quiet 6-day periods (Figures 13 and 14, respectively). Figure 13 shows densities along CHAMP and GRACE-A orbits during the 2003 Halloween storm.

The 2003 Halloween storm was one of the strongest geomagnetic storms in the 21st century with a_p reaching its maximum possible value on two occasions in a 2-day period. Figure 13 shows *Dst* at a three-hourly cadence (to line up with the HASDM dataset), but a higher resolution progression of *Dst* during this storm shows minimum values of −400 nT in the second phase of the storm (Pulkkinen et al., 2005). Note

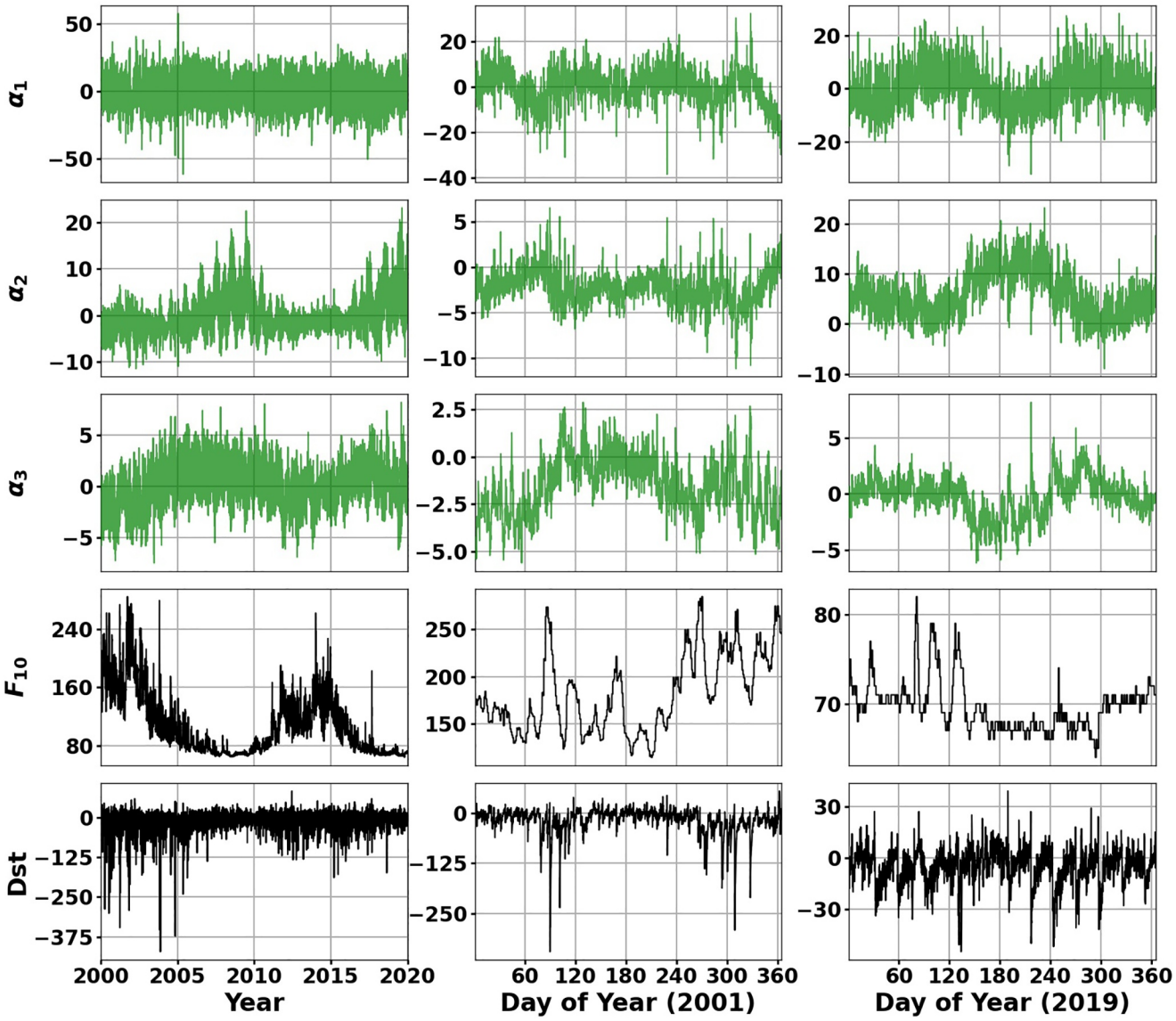

Figure 10. Temporal coefficients for the difference PCA analysis. The columns represent different time periods.

that *Dst* is multiplied by −1 in this figure to coincide with the axes for a_p. During the two density peaks, the models and satellites all have similar timing, but HASDM overpredicts relative to the satellites and JB2008.

The density recovery post-storm is modeled significantly closer to the satellites by HASDM than JB2008. We interpret this as HASDM's ability to model the impact of post-storm cooling mechanisms, such as NO. Knipp et al. (2017) showed that in shock-led geomagnetic storms, there is an overproduction of NO. Lei, Burns, et al. (2012) studied this particular storm and found that temperature and density post-storm were lower than pre-storm levels. This is observed in Figure 13 in the HASDM and satellite densities. The percent difference for JB2008 grows considerably in the recovery phase. This difference is considerably larger compared to GRACE-A than it is for CHAMP, which reinforces observations made by Oliveira and Zesta (2019). HASDM is able to capture processes like this through its calibration satellite assimilation. The mean differences for orbit-averaged densities with respect to CHAMP are 16.47% and 34.98% for HASDM and JB2008, respectively. Relative to GRACE-A, the mean differences are 23.24% and 47.51% for HASDM and JB2008,

	(2000 – 2020)			(2001)			(2019)		
	α_1	α_2	α_3	α_1	α_2	α_3	α_1	α_2	α_3
F_{10}	0.04	-0.47	-0.52	-0.19	-0.09	-0.25	0.11	-0.38	0.13
F_{81c}	0.03	-0.49	-0.53	-0.19	-0.18	-0.24	0.21	-0.45	0.19
S_{10}	0.07	-0.54	-0.53	-0.22	-0.10	-0.25	0.16	-0.19	-0.06
S_{81c}	0.06	-0.55	-0.51	-0.21	-0.16	-0.30	0.31	-0.14	-0.18
M_{10}	0.05	-0.49	-0.54	-0.19	-0.10	-0.23	0.07	-0.07	-0.15
M_{81c}	0.04	-0.50	-0.52	-0.20	-0.18	-0.27	0.24	0.09	-0.33
Y_{10}	0.05	-0.55	-0.51	-0.17	-0.07	-0.23	0.02	0.14	-0.35
Y_{81c}	0.05	-0.56	-0.50	-0.20	-0.17	-0.27	0.08	0.22	-0.40
ap	-0.06	-0.15	0.19	-0.20	0.25	0.21	-0.04	-0.17	0.39
Dst	-0.09	0.25	-0.14	-0.04	0.11	-0.27	-0.00	0.27	-0.37
$semi_{sin}$	-0.07	0.14	0.12	0.05	0.27	-0.34	-0.34	0.26	0.10
$semi_{cos}$	-0.05	0.27	-0.15	0.01	0.07	0.01	-0.37	0.44	-0.51
ann_{sin}	0.09	-0.04	-0.02	-0.05	0.28	0.10	0.09	-0.06	-0.11
ann_{cos}	0.01	-0.25	-0.10	-0.14	0.06	-0.55	0.06	-0.55	0.41

Figure 11. Heat map of the Pearson correlation coefficients between all inputs and the first three density difference PCA coefficients for: 2000–2020 (left), 2001 only (center), and 2019 only (right).

respectively. The constant bias in HASDM may be attributed to the aforementioned c_D and SRP uncertainty or errors in HASDM.

In Figure 14, the same information is presented for a quiet period in 2009. For this period, F_{10} remains at solar minimum levels, and stays between 69 and 70 *sfu*. Concurrently, a_p varies continuously but never exceeds 12 (K_p = 3-).

In the orbit-averaged plots, HASDM is discernibly closer to the satellite densities. JB2008 predicts density closer to HASDM for CHAMP (lower altitude) than for GRACE-A. Referring back to Figure 1, the difference

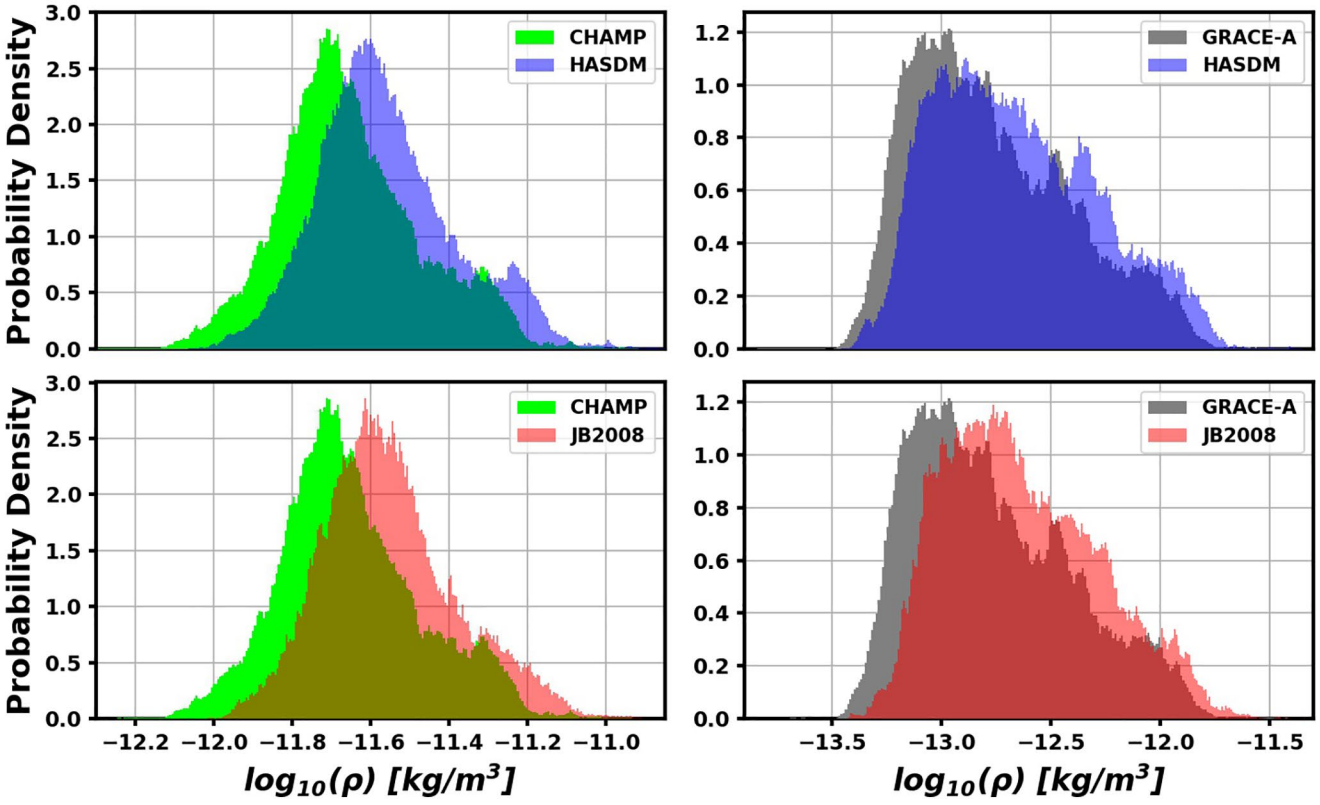

Figure 12. Histograms for CHAMP (left) and GRACE-A (right) orbits and corresponding densities from HASDM (top) and JB2008 (bottom). Values are centered averages with a window of 90 min, ~1 orbit.

Table 1
Mean Absolute Percent Difference Error Statistics for Both Models and Satellites

	CHAMP		CHAMP (OA)		GRACE-A		GRACE-A (OA)	
Year	HASDM	JB2008	HASDM	JB2008	HASDM	JB2008	HASDM	JB2008
All	29.35%	33.96%	23.84%	27.74%	41.80%	50.52%	30.93%	39.93%
2002	22.10%	24.31%	19.33%	20.44%	27.70%	29.66%	23.07%	24.63%
2003	23.04%	23.26%	19.51%	18.79%	35.91%	36.97%	29.69%	29.05%
2004	25.23%	22.88%	21.59%	18.08%	41.05%	38.04%	34.28%	30.65%
2005	28.24%	33.29%	23.96%	28.64%	45.06%	57.95%	37.09%	50.59%
2006	29.72%	39.85%	24.52%	34.48%	36.90%	53.41%	30.77%	48.44%
2007	31.33%	37.99%	25.33%	31.86%	48.20%	63.89%	30.56%	45.34%
2008	41.31%	50.44%	28.13%	35.69%	40.65%	52.55%	24.84%	38.66%
2009	33.66%	41.80%	27.95%	35.68%	49.11%	63.35%	29.19%	45.46%
2010	32.33%	24.52%	28.08%	20.59%	44.69%	41.75%	37.50%	34.26%

"OA" Denotes Orbit-averaged.

in average altitude for the satellites in 2009 is approximately 150 km. This explains the order of magnitude difference in densities and shows that HASDM more closely matches satellite estimates at higher altitudes. For both satellites' orbits, HASDM is predicting lower density than JB2008 for a majority of the period. HASDM may be better capturing the effects of radiative cooling by CO_2, not modeled by JB2008. Emmert et al. (2010) found that in the 2008 solar minimum, there were record-low densities that could not be entirely attributed to F_{10}. They identified that enhanced radiative cooling by CO_2 was a major contributor to the decreased density. HASDM's data assimilation scheme is able to make corrections based observations of lower density. The mean differences for orbit-averaged densities with respect to CHAMP are 26.47% and 36.98% for HASDM and JB2008, respectively. Regarding to GRACE-A, the mean differences are 16.01% and 36.00% for HASDM and JB2008, respectively.

There are considerable peaks in the JB2008 densities, particularly for the GRACE-A orbit. These seem to be a response to the geomagnetic activity (seen in the bottom-right panel). All JB2008 density peaks lag a_p spikes by about 12 h and deviate from HASDM and satellite densities. a_p is a good indicator of the source, because JB2008 uses a_p when no storms are detected. JB2008 is likely overestimating the impact of the a_p fluctuations relative to HASDM and considering the satellite densities.

6. Summary

In this work, we investigate HASDM and JB2008 densities by leveraging PCA. To analyze the model data, PCA was applied after normalization and centering for both models, along with the difference of the $\log_{10}$ densities. The comparison of the modes for the two models showed that HASDM likely models the presence of the winter helium bulge, unlike JB2008. The density difference PCA demonstrated HASDM's ability to model the short and long-term movement of lighter species during solar minimum, which was observed through its modes and the comparison of its temporal coefficients across the three periods of interest. Further investigation is required to confirm these observations.

By comparing the two models to CHAMP and GRACE-A accelerometer-derived density estimates, we found that HASDM had a more similar density distribution to the satellite estimates than JB2008. Overall, HASDM's predictions were closer to CHAMP's estimates (orbit = 29.35% and averaged = 23.84%) than JB2008's (orbit = 33.96% and averaged = 27.74%). This observation was also true with respect to GRACE-A:

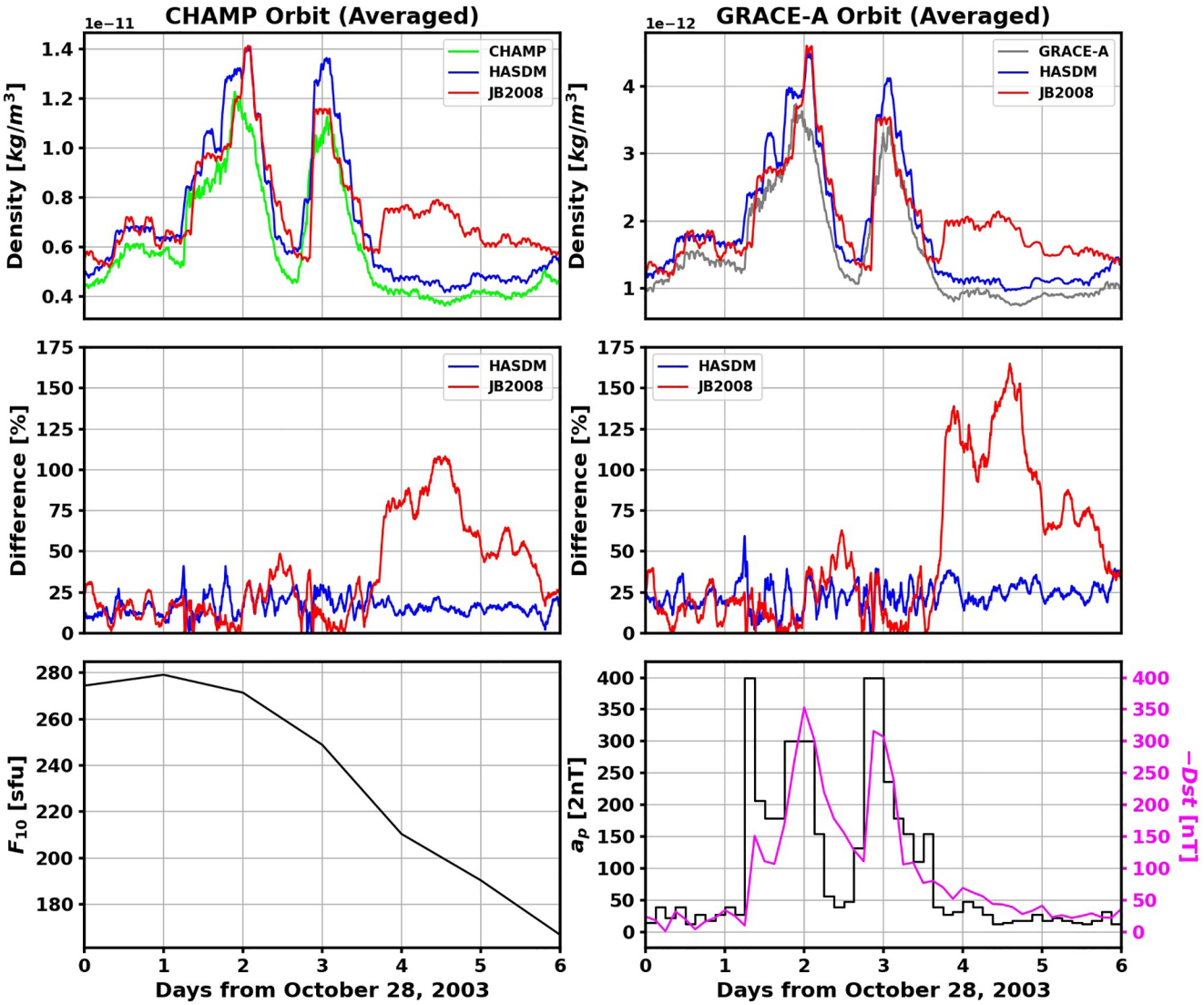

Figure 13. Densities from CHAMP, GRACE-A, HASDM, and JB2008 following a storm period in 2003. The first row shows orbit-averaged densities, with the second showing the percent differences for the orbit-averaged densities. The bottom panels show F_{10} and $a_p/-Dst$.

HASDM (orbit = 41.80% and averaged = 30.93%) JB2008 (orbit = 50.52% and averaged = 39.93%). By examining the model and satellite densities during the 2003 Halloween storm, it was observed that HASDM achieved significant improvements post-storm, capturing the over-cooled state of the thermosphere due to an overproduction of NO. The difference in density for JB2008 relative to GRACE-A reached over 150% in the 48 h period following the storm while HASDM maintained a 20%–25% difference. Looking at the densities for a quiet period, we saw that HASDM predicted lower densities than JB2008, potentially representing its ability to capture long-term cooling effects from CO_2 during solar minimum through its data assimilation scheme. Across this 6-day window, HASDM differences relative to the satellite estimates were 10%–16% lower than JB2008.

In the future, we plan to develop machine-learned (ML) models using various drivers. Not only will it generate a computationally efficient predictive model, it will allow us to perform nonlinear analysis into the contribution of these and additional drivers. These models can leverage ML techniques to also model uncertainty in the system (Licata et al., 2021). More studies of HASDM's predictions during major storms are required and detailed statistics of its prediction capability during storm phases would provide great insight

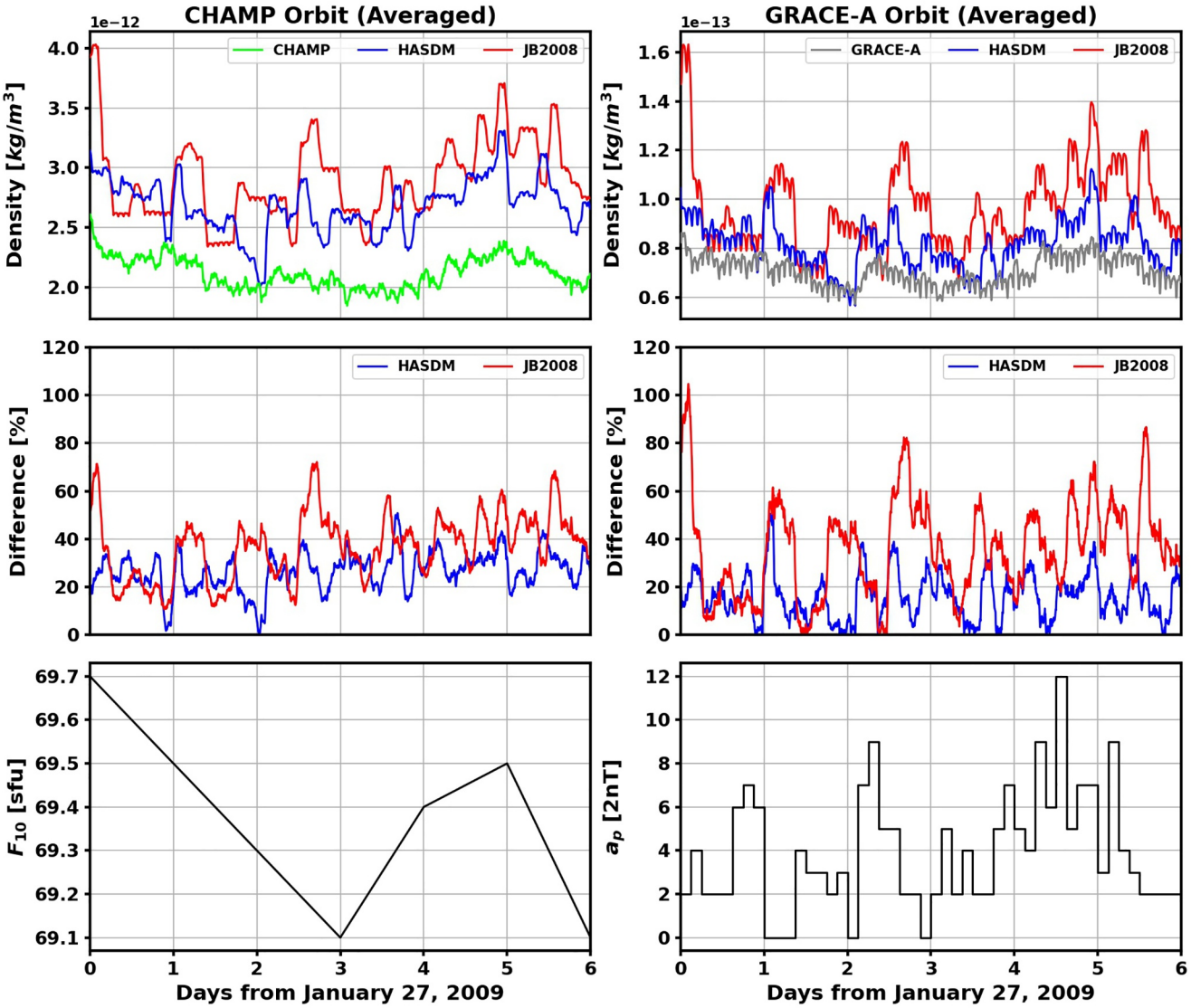

Figure 14. Densities from CHAMP, GRACE-A, HASDM, and JB2008 during a quiet period in 2009. The first row shows orbit-averaged densities, with the second showing the percent differences for the orbit-averaged densities. The bottom panels show F_{10} and a_p.

for future model development. While it is outside the scope of this work, it is necessary to further investigate HASDM's ability to capture light species movement during solar minimum.

Data Availability Statement

The JB2008 model is available for download at https://spacewx.com/jb2008/. Requests can be submitted for access to the SET HASDM density database at https://spacewx.com/hasdm/ and all reasonable requests for scientific research will be accepted as explained in the rules of road document on the website. The historical space weather indices used in this study can also be found at the JB2008 link. Original CHAMP and GRACE density estimates from Mehta et al. (2017) can be found at http://tinyurl.com/densitysets. As a product of this work, we appended the HASDM and JB2008 density estimates to those files. These updated files can be found at https://zenodo.org/record/4602380#.YEwEw-1KhuU.

Acknowledgments
This work was made possible by NASA Established Program to Stimulate Competitive Research, Grant #80NSSC19M0054. SET and WVU gratefully acknowledge support from the NASA SBIR contract #80NSSC20C0292 for Machine learning Enabled Thermosphere Advanced by HASDM (METAHASDM). The authors would like to thank the anonymous reviewers for all of their time and effort. Their feedback allowed us to significantly improve the manuscript.

References

Bettadpur, S. (2012). *Gravity recovery and climate experiment: Product specification document, GRACE 327-720, CSR-GR-03-02, cent for space research*. The University of Texas.

Bjornsson, H., & Venegas, S. A. (1997). A manual for EOF and SVD analyses of climatic data. *Technical report* (No. 97-1. Montreal, Quebec: MCGill University.

Bowman, B., & Storz, M. (2003). High accuracy satellite drag model (HASDM) review. In *AIAA/AAS Astrodynamics Specialist Conference* (AAS 03-625).

Bowman, B., Tobiska, W. K., Marcos, F., Huang, C., Lin, C., & Burke, W. (2008). A new empirical thermospheric density model JB2008 using new solar and geomagnetic indices. In *AIAA/AAS Astrodynamics Specialist Conference and Exhibit* (AIAA 2008-6438), Honolulu, Hawaii. https://doi.org/10.2514/6.2008-6438

Bruinsma, S. (2015). The DTM-2013 thermosphere model. *Journal of Space Weather and Space Climate*, *5*, A1. https://doi.org/10.1051/swsc/2015001

Bruinsma, S., Boniface, C., Sutton, E. K., & Fedrizzi, M. (2021). Thermosphere modeling capabilities assessment: Geomagnetic storms. *Journal of Space Weather and Space Climate*, *11*, 12. https://doi.org/10.1051/swsc/2021002

Cageao, R., & Kerr, R. (1984). Global distribution of helium in the upper atmosphere during solar minimum. *Planetary and Space Science*, *32*(12), 1523–1529. https://doi.org/10.1016/0032-0633(84)90019-9

Calabia, A., & Jin, S. (2016a). Assessment of conservative force models from GRACE accelerometers and precise orbit determination. *Aerospace Science and Technology*, *49*, 80–87. https://doi.org/10.1016/j.ast.2015.11.034

Calabia, A., & Jin, S. (2016b). New modes and mechanisms of thermospheric mass density variations from GRACE accelerometers. *Journal of Geophysical Research: Space Physics*, *121*(11), 11191–11212. https://doi.org/10.1002/2016JA022594

Casali, S., & Barker, W. (2002). Dynamic calibration atmosphere (DCA) for the high accuracy satellite drag model (HASDM). In *AIAA/AAS Astrodynamics Specialist Conference and Exhibit*, Monterey, CA. https://doi.org/10.2514/6.2002-4888

Covington, A. E. (1948). Solar noise observations on 10.7 centimeters. *Proceedings of the IRE*, *36*(4), 454–457. https://doi.org/10.1109/JRPROC.1948.234598

Deng, Y., Fuller-Rowell, T. J., Ridley, A. J., Knipp, D. J., & Lopez, R. E. (2013). Theoretical study: Influence of different energy sources on the cusp neutral density enhancement. *Journal of Geophysical Research: Space Physics*, *118*(5), 2340–2349. https://doi.org/10.1002/jgra.50197

Doornbos, E. (2012). *Producing density and crosswind data from satellite dynamics observations* (pp. 91–126). Berlin, Heidelberg: Springer. https://doi.org/10.1007/978-3-642-25129-0_4

Emmert, J. T (2015). Thermospheric mass density: A review. *Advances in Space Research*, *56*, 773–824. https://doi.org/10.1016/j.asr.2015.05.038

Emmert, J. T., Lean, J. L., & Picone, J. M. (2010). Record-low thermospheric density during the 2008 solar minimum. *Geophysical Research Letters*, *37*(12), L12102. https://doi.org/10.1029/2010GL043671

Fedrizzi, M., Fuller-Rowell, T. J., & Codrescu, M. V. (2012). Global Joule heating index derived from thermospheric density physics-based modeling and observations. *Space Weather*, *10*(3), S03001. https://doi.org/10.1029/2011SW000724

Ganushkina, N., Jaynes, A., & Liemohn, M. (2017). Space weather effects produced by the ring current particles. *Space Science Reviews*, *212*(3–4), 1315–1344. https://doi.org/10.1007/s11214-017-0412-2

Gondelach, D. J, & Linares, R (2020). Real-time thermospheric density estimation via two-line element data assimilation. *Space Weather*, *18*(2), e2019SW002. https://doi.org/10.1029/2019sw002356

Hotelling, H. (1933). Analysis of a complex of statistical variables into principal components. *Journal of Educational Psychology*, *24*(6), 417–441. https://doi.org/10.1037/h0071325

Houghton, J. T. (1970). Absorption and emission by carbon-dioxide in the mesosphere. *Quarterly Journal of the Royal Meteorological Society*, *96*(410), 767–770. https://doi.org/10.1002/qj.49709641025

Jacchia, L. G. (1970). New Static Models of the Thermosphere and Exosphere with Empirical Temperature Profiles (p. 313). SAO Special Report.

Karl Pearson, F. R. S. (1901). LIII. On lines and planes of closest fit to systems of points in space. *The London, Edinburgh, and Dublin Philosophical Magazine and Journal of Science*, *2*(11), 559–572. https://doi.org/10.1080/14786440109462720

Keating, G. M., & Prior, E. J. (1968). The winter helium bulge, in space research VIII. In: A. P. Mithra, L. G. Jacchia, & W. S. Newman, (Eds.), *Proceedings of the tenth COSPAR plenary meeting* (pp. 982–992). London: Imperial College of Science and Technology.

Kessler, D. J., & Cour-Palais, B. G. (1978). Collision frequency of artificial satellites: The creation of a debris belt. *Journal of Geophysical Research: Space Physics*, *83*(A6), 2637–2646. https://doi.org/10.1029/JA083iA06p02637

Knipp, D. J., Pette, D. V., Kilcommons, L. M., Isaacs, T. L., Cruz, A. A., Mlynczak, M. G., et al. (2017). Thermospheric nitric oxide response to shock-led storms. *Space Weather*, *15*(2), 325–342. https://doi.org/10.1002/2016SW001567

Kockarts, G. (1980). Nitric oxide cooling in the terrestrial thermosphere. *Geophysical Research Letters*, *7*(2), 137–140. https://doi.org/10.1029/GL007i002p00137

Lei, J., Burns, A. G., Thayer, J. P., Wang, W., Mlynczak, M. G., Hunt, L. A., et al. (2012). Overcooling in the upper thermosphere during the recovery phase of the 2003 October storms. *Journal of Geophysical Research: Space Physics*, *117*(A3), A03314. https://doi.org/10.1029/2011JA016994

Lei, J., Matsuo, T., Dou, X., Sutton, E., & Luan, X. (2012). Annual and semiannual variations of thermospheric density: EOF analysis of CHAMP and GRACE data. *Journal of Geophysical Research: Space Physics*, *117*(A1), A01310. https://doi.org/10.1029/2011JA017324

Licata, R. J., Mehta, P., & Tobiska, W. K. (2021). Impact of driver and model uncertainty on drag and orbit prediction. In Proceedings of the 31st AAS/AIAA Space Flight Mechanics Meeting, Napa, CA.

Licata, R. J., Tobiska, W. K., & Mehta, P. M. (2020). Benchmarking forecasting models for space weather drivers. *Space Weather*, *18*(10), 496. https://doi.org/10.1029/2020SW002496

Luhr, H., Grunwaldt, L., & Forste, C. (2002). CHAMP reference systems, transformations and standards. Technical report (CH-GFZ-RS-002), Postdam, Germany: GFZ-Potsdam.

Marcos, F., Kendra, M., Griffin, J., Bass, J., Larson, D., & Liu, J. J. (1998). Precision low earth orbit determination using atmospheric density calibration. *Journal of the Astronautical Sciences*, *46*, 395–409. https://doi.org/10.1007/bf03546389

Matsuo, T., & Forbes, J. M. (2010). Principal modes of thermospheric density variability: Empirical orthogonal function analysis of CHAMP 2001–2008 data. *Journal of Geophysical Research: Space Physics*, *115*(A7), A07309. https://doi.org/10.1029/2009JA015109

Mehta, P. M., & Linares, R. (2017). A methodology for reduced order modeling and calibration of the upper atmosphere. *Space Weather*, *15*(10), 1270–1287. https://doi.org/10.1002/2017sw001642

Mehta, P. M., Linares, R., & Sutton, E. K. (2018). A quasi-physical dynamic reduced order model for thermospheric mass density via Hermitian space-dynamic mode decomposition. *Space Weather*, *16*(5), 569–588. https://doi.org/10.1029/2018SW001840

Mehta, P. M., Linares, R., & Sutton, E. K. (2019). Data-driven inference of thermosphere composition during solar minimum conditions. *Space Weather*, *17*(9), 1364–1379. https://doi.org/10.1029/2019SW002264

Mehta, P. M., McLaughlin, C. A., & Sutton, E. K. (2013). Drag coefficient modeling for grace using direct simulation Monte Carlo. *Advances in Space Research*, *52*(12), 2035–2051. https://doi.org/10.1016/j.asr.2013.08.033

Mehta, P. M., Walker, A., McLaughlin, C. A., & Koller, J. (2014). Comparing physical drag coefficients computed using different gas–surface interaction models. *Journal of Spacecraft and Rockets*, *51*(3), 873–883. https://doi.org/10.2514/1.A32566

Mehta, P. M., Walker, A. C., Sutton, E. K., & Godinez, H. C. (2017). New density estimates derived using accelerometers on board the CHAMP and GRACE satellites. *Space Weather*, *15*(4), 558–576. https://doi.org/10.1002/2016SW001562

Mlynczak, M., Martin-Torres, F. J., Russell, J., Beaumont, K., Jacobson, S., Kozyra, J., et al. (2003). The natural thermostat of nitric oxide emission at 5.3 μm in the thermosphere observed during the solar storms of April 2002. *Geophysical Research Letters*, *30*(21), 2100. https://doi.org/10.1029/2003GL017693

Nazarenko, A., Cefola, P., & Yurasov, V. (1998). Estimating atmospheric density variations to improve LEO orbit prediction accuracy. In *AIAA/AAS Space Flight Mechanics Meeting* (pp. 98–190). AAS.

Oliveira, D. M., & Zesta, E. (2019). Satellite orbital drag during magnetic storms. *Space Weather*, *17*(11), 1510–1533. https://doi.org/10.1029/2019SW002287

Pearson, K. (1920). Notes on the history of correlation. *Biometrika*, *13*(1), 25–45. https://doi.org/10.1093/biomet/13.1.25

Picone, J. M., Emmert, J. T., & Drob, D. P. (2016). Consistent static models of local thermospheric composition profiles.*Space Physics*, arXiv.

Picone, J. M., Hedin, A. E., Drob, D. P., & Aikin, A. C. (2002). NRLMSISE-00 empirical model of the atmosphere: Statistical comparisons and scientific issues. *Journal of Geophysical Research: Space Physics*, *107*(A12), SIA 15-1–SIA 15-16. https://doi.org/10.1029/2002ja009430

Pulkkinen, A., Lindahl, S., Viljanen, A., & Pirjola, R. (2005). Geomagnetic storm of 29–31 October 2003: Geomagnetically induced currents and their relation to problems in the Swedish high-voltage power transmission system. *Space Weather*, *3*(8), S08C03. https://doi.org/10.1029/2004sw000123

Qian, L., & Solomon, S. (2012). Thermospheric density: An overview of temporal and spatial variations. *Space Science Reviews*, *168*, 147–173. https://doi.org/10.1007/s11214-011-9810-z

Reber, C. A., & Hays, P. B. (1973). Thermospheric wind effects on the distribution of helium and argon in the Earth's upper atmosphere. *Journal of Geophysical Research*, *78*(16), 2977–2991. https://doi.org/10.1029/JA078i016p02977

Storz, M., Bowman, B., & Branson, J. (2005). High accuracy satellite drag model (HASDM). In *AIAA/AAS Astrodynamics Specialist Conference and Exhibit*, Monterey, CA. https://doi.org/10.2514/6.2002-4886

Sutton, E. K. (2008). *Effects of solar disturbances on the thermosphere densities and winds from CHAMP and GRACE satellite accelerometer data* (PhD thesis). University of Colorado at Boulder.

Sutton, E. K. (2016). Interhemispheric transport of light neutral species in the thermosphere. *Geophysical Research Letters*, *43*(24), 12325–12332. https://doi.org/10.1002/2016gl071679

Thayer, J. P., Liu, X., Lei, J., Pilinski, M., & Burns, A. G. (2012). The impact of helium on thermosphere mass density response to geomagnetic activity during the recent solar minimum. *Journal of Geophysical Research: Space Physics*, *117*(A7), A07315. https://doi.org/10.1029/2012JA017832

Tobiska, W. K., Bouwer, S. D., & Bowman, B. R. (2008). The development of new solar indices for use in thermospheric density modeling. *Journal of Atmospheric and Solar-Terrestrial Physics*, *70*(5), 803–819. https://doi.org/10.1016/j.jastp.2007.11.001

Tobiska, W. K., Bowman, B., & Bouwer, S. D. (2008). *Solar and geomagnetic indices for the JB2008 thermosphere density model* (Chap. 4). COSPAR CIRA Draft.

Tobiska, W. K., Bowman, B. R., Bouwer, D., Cruz, A., Wahl, K., Pilinski, M., et al. (2021). The SET HASDM Density Database. *Space Weather*, *19*, e2020SW002682. https://doi.org/10.1029/2020SW002682

Tobiska, W. K., Knipp, D. J., Burke, W. J., Bouwer, D., Bailey, J., Odstrcil, D., et al. (2013). The *Anemomilos* prediction methodology for Dst. *Space Weather*, *11*(9), 490–508. https://doi.org/10.1002/swe.20094

Tobiska, W. K., Woods, T., Eparvier, F., Viereck, R., Floyd, L., Bouwer, D., et al. (2000). The SOLAR2000 empirical solar irradiance model and forecast tool. *Journal of Atmospheric and Solar-Terrestrial Physics*, *62*(14), 1233–1250. https://doi.org/10.1016/s1364-6826(00)00070-5

Vickers, H., Kosch, M. J., Sutton, E., Bjoland, L., Ogawa, Y., & La Hoz, C. (2014). A solar cycle of upper thermosphere density observations from the EISCAT Svalbard Radar. *Journal of Geophysical Research: Space Physics*, *119*(8), 6833–6845. https://doi.org/10.1002/2014ja019885

Vielberg, K., & Kusche, J. (2020). Extended forward and inverse modeling of radiation pressure accelerations for LEO satellites. *Journal of Geodesy*, *94*, 43. https://doi.org/10.1007/s00190-020-01368-6

Walker, A., Mehta, P., & Koller, J. (2014). Drag coefficient model using the Cercignani–Lampis–Lord gas–surface interaction model. *Journal of Spacecraft and Rockets*, *51*(5), 1544–1563. https://doi.org/10.2514/1.A32677

Weimer, D. R, Mehta, P. M, Tobiska, W. K., Doornbos, E., Mlynczak, M. G., Drob, D. P., & Emmert, J. T. (2020). Improving neutral density predictions using exospheric temperatures calculated on a geodesic, polyhedral grid. *Space Weather*, *18*(1), 355. https://doi.org/10.1029/2019SW002355